Shock Capturing Techniques for Compressible Inviscid Flow in the Context of Hybridizable Discontinuous Galerkin Method

Ahmed Sherif

January 3, 2018

Abstract

In the context of computational fluid dynamics, solving problems that include shocks numerically requires an extra effort in order to capture the shocks accurately avoiding any numerical oscillations. To this end, shock-capturing techniques are used. One of the famous techniques is the artificial viscosity method where extra diffusion is added only near the shocks to stabilize the solution. Thus, two main ingredients of this technique are the shock-sensor to determine the shock location and the amount of diffusion added nearby. The main purpose of this work is: First, to demonstrate the shock-capturing technique using artificial viscosity method. Second, to show a comparison between two different shock-sensors. In this report, the analytical solution of Sod's shock tube problem is used to demonstrate the features detected by each of the two shock-sensors.

Keywords: Euler equations, shock-capturing, artificial viscosity method.

1 Introduction

The compressible inviscid flow governed by Euler equations is a system of non-linear hyperbolic partial differential equations. In non-linear hyperbolic problems, discontinuities in the solution can be generated, which is known as shock waves in the context of fluid flow, even if the the initial conditions of the problem are continuous [1, Chap. 4]. It is known that the presence of such discontinuities in the solution makes the numerical computation more complicated especially when higher-order spatial discretization ($k > 1$) is utilised [2]. The reason behind this is the appearance of non-physical superior oscillations in the solution near the discontinuities. The introduction of shock-capturing techniques to eliminate the arising oscillations and obtain a good structure of the shocks or discontinuities is then a must.

There are many approaches to resolve a shock, a straightforward approach is to reduce the order of approximation to $k = 1$ near the shock and refine the mesh nearby [3], but this approach is very computationally expensive because very fine meshes are needed. Another approach is the limiting techniques [4]. The extension of limiting techniques to discontinuous Galerkin (DG) methods has become very popular approach for shock-capturing in DG, see for example [2, 5, 6]. Their main disadvantages are that the order of approximation is reduced near the shock leading to degradation of accuracy, their extension to multiple dimensions is not straightforward, they present some difficulties for implicit time-marching schemes, and they are usually tied to specific element shapes and integration quadratures.

There are many approaches that are not mentioned in this work, but the main idea of using a shock-capturing technique is to compensate the reduction in diffusion resulting from using higher-order discretization. In this report, a very simple technique using artificial viscosity is exploited, this approach was first introduced by Von Neumann and Richtmyer [7].

2 Artificial Viscosity Method

The governing partial differential equation for Euler flow is [1, Chap. 1]:

$$\frac{\partial \boldsymbol{U}}{\partial t} + \boldsymbol{\nabla} \cdot \boldsymbol{F} = \boldsymbol{S} \tag{2.1}$$

where $\boldsymbol{U} = (\rho, \rho \boldsymbol{v}^T, \rho E)^T$ is the vector of conservative variables, $\boldsymbol{F}$ is the advection flux tensor, and $\boldsymbol{S}$ is a source vector. Note that ρ is the density, $\rho \boldsymbol{v}$ is the momentum, and ρE is the total energy. By adding artificial diffusion to Euler equations, the modified partial differential equation is written as:

$$\frac{\partial \boldsymbol{U}}{\partial t} + \boldsymbol{\nabla} \cdot \boldsymbol{F} - \boldsymbol{\nabla} \cdot \boldsymbol{G} = \boldsymbol{S} \tag{2.2}$$

where $\boldsymbol{G}$ is the viscous flux tensor. In this work two definitions for $\boldsymbol{G}$ are used and they are given as:

- *Laplacian* viscous flux:

$$\boldsymbol{G} = \epsilon \boldsymbol{\nabla} U \tag{2.3}$$

- *Enthalpy-preserving* viscous flux:

$$\boldsymbol{G} = \epsilon \boldsymbol{\nabla} U_H \tag{2.4}$$

where $\boldsymbol{U}_H = (\rho, \rho\boldsymbol{v}^T, \rho H)^T$ given that H is the enthalpy. Note that ϵ is the amount of added viscosity or diffusion.

It is important to note that the diffusion term is added only near the shock and not everywhere in the domain. Thus, it is crucial to detect the position of the shock which is done using a shock-sensor or sometimes called a discontinuity-sensor.

2.1 Amount of Artificial Viscosity

Selecting the amount of viscosity to be added to the equation is not trivial. The goal is to get a sharp structure of the shock buy yet resolvable, and only add viscosity near the shock. To this end, the two main ingredients of the shock-capturing techniques are the shock-sensor s_ϵ and the sensor dependent viscosity ϵ.

The viscosity ϵ should have the units of velocity times length, thus it is defined as:

$$\epsilon = l_{scale} v_{scale} f(s_\epsilon) \tag{2.5}$$

where l_{scale} and v_{scale} are the length and velocity scales, respectively, and $f(s_\epsilon)$ is a dimensionless switch function depending on the sensor s_ϵ. The velocity scale is defined following the work in [8] as:

$$v_{scale} = \sqrt{\boldsymbol{v} \cdot \boldsymbol{v} + c^2} \tag{2.6}$$

2.2 Shock-Sensor

As mentioned earlier, the shock-sensor is one of the two ingredients for any shock-capturing technique. In this work, two different sensors are compared. The first sensor introduced by Persson and Peraire in [9] is called Resolution Indicator sensor, and the second one introduced by Barter and Darmofal in [10] is called Dilatation-Based sensor.

***Persson-Peraire* sensor/ Resolution indicator sensor**

Following the work of Persson and Peraire in [9] and Casoni in [11], the shock-sensor is defined as:

$$s_\epsilon(\rho) = \frac{\boldsymbol{\rho}^T \boldsymbol{V}^{-T} \boldsymbol{P}_H \boldsymbol{V}^{-1} \boldsymbol{\rho}}{\boldsymbol{\rho}^T \boldsymbol{V}^{-T} \boldsymbol{V}^{-1} \boldsymbol{\rho}} \tag{2.7}$$

where $\boldsymbol{\rho}$ is the vector of nodal values of ρ, $\boldsymbol{V}$ is the Vandermonde matrix, see for example [12,13], and $\boldsymbol{P}_H$ is an orthonormal projection matrix onto the space of monomials of degree k, see [11] for more details.

The switch function $f(s_\epsilon)$ is defined as

$$f(s_\epsilon) = \begin{cases} 0 & \text{if} \quad \log_{10} s_\epsilon < s_0 - \kappa \\ \dfrac{1}{2}\left(1 + \sin\dfrac{\pi(\log_{10} s_\epsilon - s_0)}{2\kappa}\right) & \text{if} \quad s_0 - \kappa < \log_{10} s_\epsilon < s_0 + \kappa \\ 1 & \text{if} \quad s_0 + \kappa < \log_{10} s_\epsilon \end{cases} \qquad (2.8)$$

where $s_0 = -6\log_{10} k$ and $\kappa = 2\log_{10} k$.

Barter and Darmofal showed the importance of having a continuous artificial viscosity field, thus the length scale is smoothed $l_{scale} = h(\boldsymbol{x})/k$, and the switch function $f(s_\epsilon)$ is smoothed as well. Note that $h(\boldsymbol{x})$ is a piece-wise linear reconstruction of the minimum element size obtained by averaging the minimum size, h^e, of all the elements surrounding a vertex.

The Resolution Indicator sensors is robust and very accurate for high-order elements. It does not only deal with shock waves, but can also detect some other discontinuities, such as expansion corners. However, the sensor is not smooth and its linearisation is quite complicated [14].

Dilatation-Based sensor

Following the work of Barter and Darmofal in [10] and Moro in [8], the shock-sensor is defined as:

$$s_\epsilon = -k_h \frac{h(\boldsymbol{x})}{k}\frac{\boldsymbol{\nabla}\cdot\boldsymbol{v}}{c^*} \qquad (2.9)$$

where $k_h \in [1, 2]$ is a correction factor, $\boldsymbol{v}$ is the velocity vector, and c^* is the critical speed of sound defined as:

$$c^* = \sqrt{\gamma R T_0 \frac{2}{\gamma + 1}} \qquad (2.10)$$

The length scale is defined as $l_{scale} = k_h h(\boldsymbol{x})/k$ and the switch function $f(s_\epsilon)$ is defined as

$$f(s_\epsilon) = \frac{\log(1 + e^{\alpha(s_\epsilon - \beta)})}{\alpha} \qquad (2.11)$$

where $\alpha = 10^4$ and $\beta = 0.01$.

The Dilatation-Based sensor is robust, smooth, and defined pointwise. Its implementation is simple, and can be easily linearised to solve the non-linear problem using a Newton-Raphson algorithm. However, being designed to deal only with shocks, other methods are needed when the problems include other strong discontinuities, such as in an expansion corner [14].

3 Understanding Shock-Capturing by an Example

In this section, a comparison between the two discontinuity sensors, *Persson-Peraire* and *Dilatation-Based*, is done to show the flow features captured by each sensor. Once a discontinuity is detected, artificial viscosity is added nearby to capture a good structure of this discontinuity. Artificial viscosity is added near discontinuities because higher-order polynomial interpolation of discontinuous solution results in superior numerical oscillations. A detailed study is done for Sod's shock tube problem to further understand the previous statements.

3.1 Sod's Shock Tube Problem Analysis

Sod's shock tube is a classical problem with known exact solution used to validate numerical schemes developed for solving Euler equations. It is an interesting problem because it has three important ingredients that might exist in complicated fluid flow problems, the three ingredients are: shock wave, contact discontinuity and expansion fan (rarefaction wave). Those three waves are steadily moving waves.
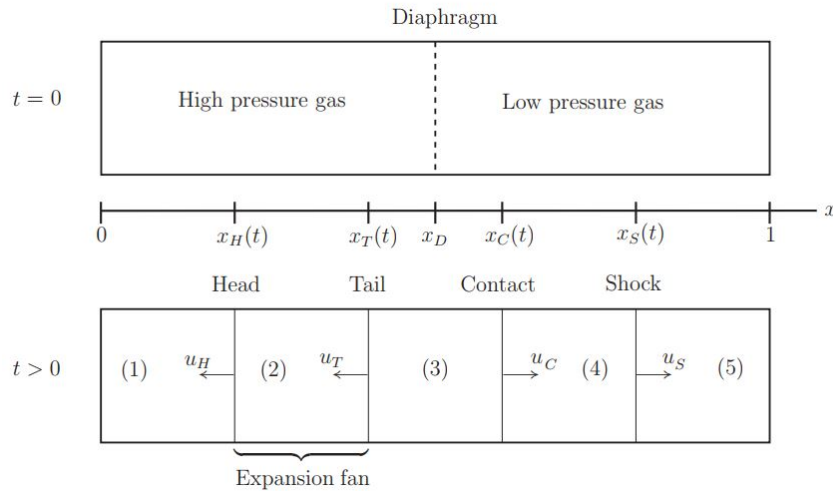

Figure 1: Shock tube problem, initial condition (top) and after diaphragm failure (bottom)

Consider a domain $\Omega = [0, 1] \times [0, 0.4]$, of slip-wall boundaries. Initially a diaphragm placed at $x_D = 0.5$ is separating two fluids, the fluid on left is a stationary high pressure and density ($p_1 = 1, \rho_1 = 1$) fluid and the one on right is a stationary low pressure and density ($p_2 = 1/3, \rho_2 = 1/3$) fluid. At time $t = 0$, the diaphragm fails and the three waves start moving as seen in Figure 1, which results in five sections where the analytical solution is already known up to the point in time when either the shock wave or the rarefaction wave is reflected by the respective ends of the shock tube [13].

5

At time $t = 0.1$, the positions of the three waves are plotted on a coarse mesh as shown in Figure 2, where the blue and red lines are the expansion fan head and tail, respectively, the yellow line represents the contact discontinuity while the purple line is the position of the shock wave. It should be noted that the analytical solution at the head and tail of the expansion fan is weakly discontinuous (continuous variables - discontinuous derivatives) and it is strongly discontinuous (discontinuous variables) at the contact and shock waves.
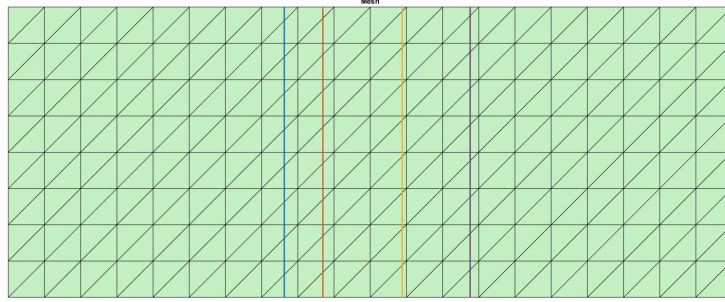
Figure 2: The positions of the three waves at time $t = 0.1$ plotted on top of a coarse mesh

Using elements of order $p = 3$, the analytical solution is computed at all the nodes, and the solution within elements is interpolated using the standard finite element polynomial approximation. As mentioned earlier, approximating discontinuous solutions using higher-order polynomials results in numerical oscillations near the discontinuities, which can be clearly seen, for instance, in the interpolated solution of density and velocity shown in Figure 3. Now, it is clearly understood the reason why a shock capturing technique is needed for higher-order elements.

The shock capturing technique is composed of two main ingredients, a discontinuity sensor and addition of artificial viscosity. Figure 4 shows the features detected by each of the two discontinuity sensors, *Persson-Peraire* and *Dilatation-Based*, when applied to the solution shown in Figure 3, it also shows the amount of added artificial viscosity in terms of the maximum per element, i.e. the viscosity is computed at all the Gauss points of an element and only the maximum value among them is shown. It is observed that *Persson-Peraire* sensor detects both shock and contact discontinuity because of the high density gradient nearby, it doesn't detect the expansion fan because the density is more smooth nearby. More viscosity is added near the shock than near the contact because of the higher density gradient near the shock. On the other hand, the *Dilatation-Based* sensor detects both shock and expansion fan, it adds much more artificial viscosity to the shock compared to the expansion fan, the reason is the higher divergence of velocity near the shock, it doesn't detect the contact discontinuity because the velocity is divergence free at the contact. It is also observed that *Dilatation-Based* sensor leads to addition of more artificial viscosity to the shock compared to the case of *Persson-Peraire*, more than ten times the amount of viscosity. Furthermore, in case of *Dilatation-Based*, the artificial viscosity is added only to the elements with discontinuities in the solution, while in the case of *Persson-Peraire*, the artificial viscosity is added also to the adjacent elements.
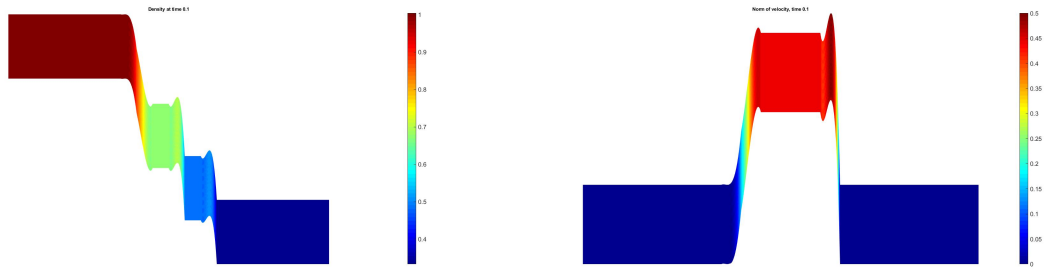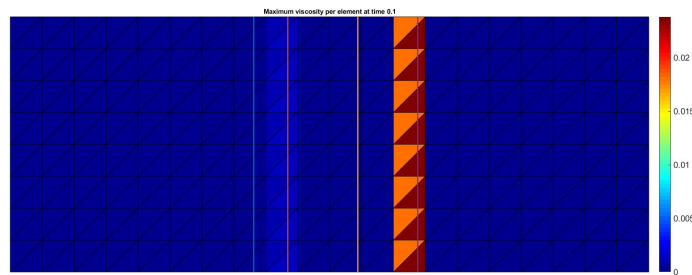
(a) Density   (b) Velocity

Figure 3: The cubic polynomial interpolation of the analytical nodal values of density and velocity at time $t = 0.1$ in the coarse mesh
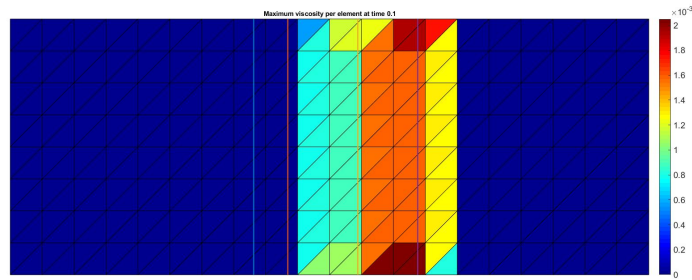
(a) Case: *Persson-Peraire* - maximum value: 2.049e-03

(b) Case: *Dilatation-Based* - maximum value: 2.381e-02

Figure 4: The maximum added artificial viscosity per element in the case of using *Persson-Peraire* and *Dilatation-Based* for the coarse mesh and elements of order $p = 3$

Another analysis is performed to understand the effect of h-refinement and p-refinement on the discontinuity sensing and the addition of artificial viscosity. First, h-refinement is considered where fine mesh shown in Figure 5 is used for the analysis. Similar to what was done for the coarse mesh, the polynomial interpolation, of the analytical nodal values of the solution, within elements is shown in Figure 6 where the numerical oscillations near the discontinuities is also observed. By refining the mesh, it is observed in Figure 7 that the amount of added viscosity is slightly increased in the case of *Persson-Peraire*, the reason could be the increase in the density gradient near the discontinuities. On the other hand, in the case of *Dilatation-Based*, the amount of added viscosity is reduced nearly four times compared to the case of coarse mesh, the reason could be the reduction in the length scale used to compute the amount of viscosity. Note that in Figure 7b, the amount of added viscosity at the expansion fan is very small, order (1e-04) near the head and (1e-07) near the tail.
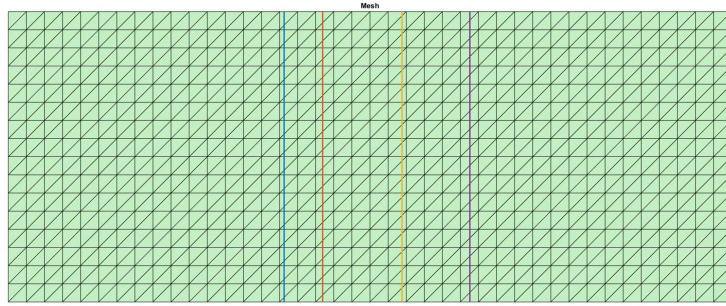

Figure 5: The positions of the three waves at time $t = 0.1$ plotted on top of a fine mesh
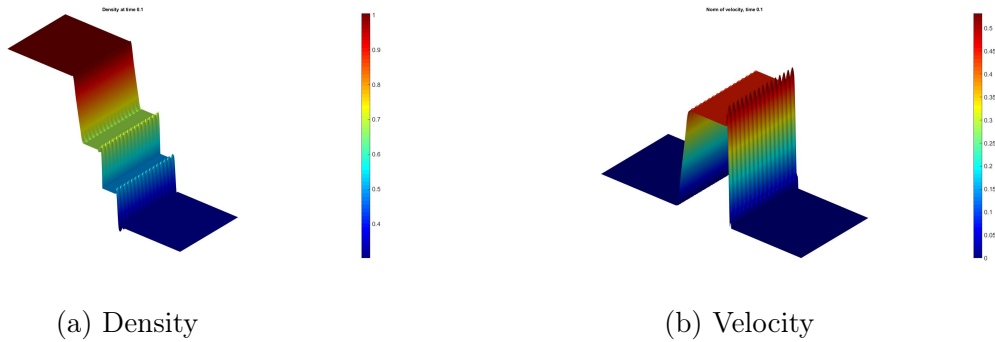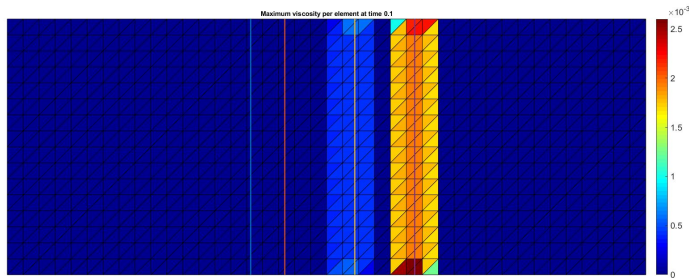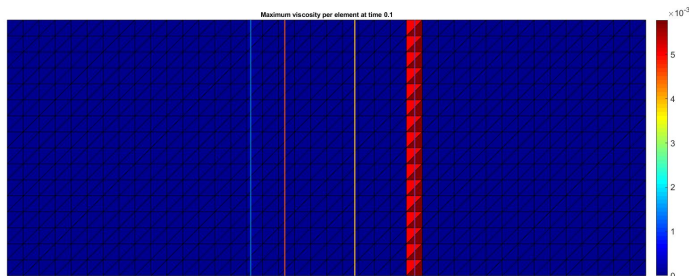

(a) Density

(b) Velocity

Figure 6: The cubic polynomial interpolation of the analytical nodal values of density and velocity at time $t = 0.1$ in the fine mesh

(a) Case: *Persson-Peraire* - maximum value: 2.600e-03

(b) Case: *Dilatation-Based* - maximum value: 5.779e-03

Figure 7: The maximum added artificial viscosity per element in the case of using *Persson-Peraire* and *Dilatation-Based* for the fine mesh and elements of order $p = 3$

Second, a p-refinement is considered, where the order of polynomial approximation is increased from $p = 3$ to $p = 4$. The analysis is done using the fine mesh shown earlier in Figure 5. It is observed in Figure 9 that the amount of added viscosity is slightly increased in the case of *Persson-Peraire* compared to the lower-order, the reason could be the higher numerical oscillations in the density appearing in 8a compared to 6a. On the other hand, in the case of *Dilatation-Based*, the amount of added viscosity is slightly reduced compared to the lower-order, the reason could be the reduction in the length scale used to compute the amount of viscosity, another reason could be the lower divergence of velocity across the shock as seen in 8b where the velocity changes from nearly 0.5 to 0, while for the lower-order, velocity changes from nearly 0.53 to 0 as seen in 6b. Note that in Figure 9b, the amount of added viscosity at the expansion fan is very small, order (1e-04) near the head and (1e-05) near the tail.
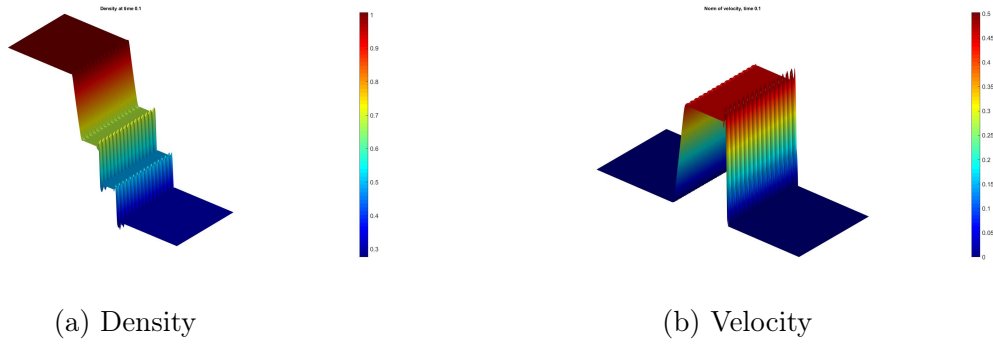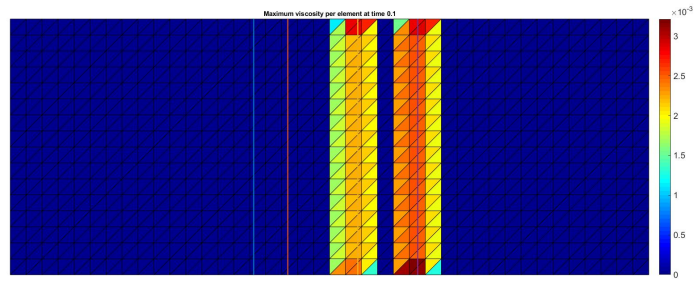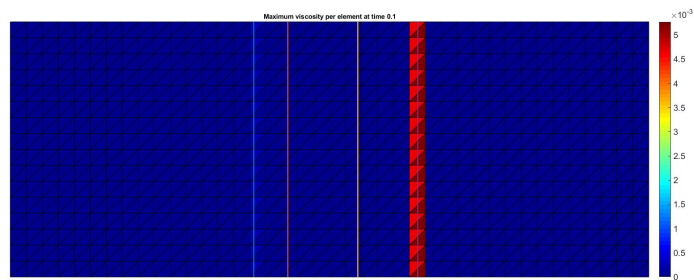
(a) Density   (b) Velocity

Figure 8: The quartic polynomial interpolation of the analytical nodal values of density and velocity at time $t = 0.1$ in the fine mesh

(a) Case: *Persson-Peraire* - maximum value: 3.213e-03

(b) Case: *Dilatation-Based* - maximum value: 5.270e-03

Figure 9: The maximum added artificial viscosity per element in the case of using *Persson-Peraire* and *Dilatation-Based* for the fine mesh and elements of order $p = 4$

4 Conclusions

As a conclusion of the work presented, the shock-capturing technique using artificial viscosity method is discussed. Two different shock-sensors were exploited, and a simple method to compute the amount of added viscosity is explained. A brief study is done on the analytical solution of Sod's tube problem to compare the two sensors being studied. Furthermore, the effect of h-refinement and p-refinement on the amount of added viscosity was shown. It is concluded that the Resolution Indocator sensor can work for any kind of discontinuity in the solution, i.e. shocks, expansion fans, and contact discontinuities. On the other hand, the Dilatation-Based sensor works only for shocks but not other types of strong discontinuities such as the contact discontinuity. Next, It is worth exploring the effect of using this approach on a more complex problems such as the transonic and supersonic flows around aerofoils.

References

[1] J. Donea and A. Huerta, *Finite element methods for flow problems*. Chichester: John Wiley & Sons, 2003.

[2] B. Cockburn and C.-W. Shu, "TVB Runge-Kutta local projection discontinuous Galerkin finite element method for conservation laws. II. General framework," *Mathematics of computation*, vol. 52, no. 186, pp. 411–435, 1989.

[3] C. E. Baumann and J. Tinsley Oden, "An adaptive-order discontinuous Galerkin method for the solution of the Euler equations of gas dynamics," *International Journal for Numerical Methods in Engineering*, vol. 47, no. 1-3, pp. 61–73, 2000.

[4] R. J. LeVeque, *Numerical methods for conservation laws*. Basel: Birkhäuser-Verlag, second ed., 1992.

[5] L. Krivodonova, "Limiters for high-order discontinuous Galerkin methods," *Journal of Computational Physics*, vol. 226, no. 1, pp. 879–896, 2007.

[6] B. Cockburn, S. Hou, and C.-W. Shu, "The Runge-Kutta local projection discontinuous Galerkin finite element method for conservation laws. IV. The multidimensional case," *Mathematics of Computation*, vol. 54, no. 190, pp. 545–581, 1990.

[7] J. VonNeumann and R. D. Richtmyer, "A method for the numerical calculation of hydrodynamic shocks," *Journal of applied physics*, vol. 21, no. 3, pp. 232–237, 1950.

[8] D. Moro, N. C. Nguyen, and J. Peraire, "Dilation-based shock capturing for high-order methods," *International Journal for Numerical Methods in Fluids*, vol. 82, no. 7, pp. 398–416, 2016.

[9] P.-O. Persson and J. Peraire, "Sub-cell shock capturing for discontinuous Galerkin methods," *AIAA paper*, vol. 112, p. 2006, 2006.

[10] G. E. Barter and D. L. Darmofal, "Shock capturing with PDE-based artificial viscosity for DGFEM: Part I. Formulation," *Journal of Computational Physics*, vol. 229, no. 5, pp. 1810–1827, 2010.

[11] E. Casoni, *Shock capturing for discontinuous Galerkin methods*. PhD thesis, Universitat Politècnica de Catalunya, 2011.

[12] J. S. Hesthaven and T. Warburton, *Nodal discontinuous Galerkin methods: algorithms, analysis, and applications*. Springer Science & Business Media, 2007.

[13] R. Sevilla, *NURBS-Enhanced Finite Element Method (NEFEM)*. PhD thesis, Universitat Politècnica de Catalunya, July 2009.

[14] X. Coll, "Hybridizable Discontinuous Galerkin method for the Compressible Euler Equations," 2017.